Journal of Colloid and Interface Science 553 (2019) 320–327

Contents lists available at ScienceDirect

Journal of Colloid and Interface Science

journal homepage: www.elsevier.com/locate/jcis

Regular Article

Embedding $CoMoO_4$ nanoparticles into porous electrospun carbon nanofibers towards superior lithium storage performance

Sanmu Xie [a], Hongkang Wang [a,*], Tianhao Yao [a], Jinkai Wang [a], Chundong Wang [c], Jian-Wen Shi [a], Xiaogang Han [a], Tianxi Liu [b], Yonghong Cheng [a]

[a] State Key Lab of Electrical Insulation and Power Equipment, Center of Nanomaterials for Renewable Energy (CNRE), School of Electrical Engineering, Xi'an Jiaotong University, Xi'an 710049, People's Republic of China
[b] State Key Laboratory for Modification of Chemical Fibers and Polymer Materials, College of Materials Science and Engineering, Donghua University, Shanghai 201620, People's Republic of China
[c] School of Optical and Electronic Information, Huazhong University of Science and Technology, Wuhan 430074, People's Republic of China

GRAPHICAL ABSTRACT

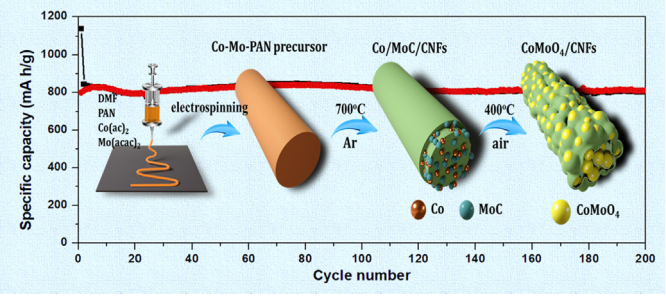

ARTICLE INFO

Article history:
Received 30 April 2019
Revised 10 June 2019
Accepted 11 June 2019
Available online 12 June 2019

Keywords:
$CoMoO_4$
Electrospinning
Porous carbon nanofibers
Lithium ion batteries
Superior electrochemical properties

ABSTRACT

$CoMoO_4$ nanoparticles have been successfully in-situ formed and simultaneously embedded within the porous carbon nanofibers ($CoMoO_4$/CNFs) *via* a facile electrospinning-annealing strategy. The porous $CoMoO_4$/CNFs exhibit a specific surface area of 255.3 m^2/g and a pore volume of 0.52 cc/g with average pore diameter of 43.5 nm. The carbon content in the $CoMoO_4$/CNFs can be readily controlled by adjusting the annealing temperature. When examined as anode materials for lithium ion batteries (LIBs), the $CoMoO_4$/CNFs demonstrate superior electrochemical performance, delivering a high reversible capacity of 802 mA h/g after 200 cycles at 200 mA/g and a high-rate capacity of 574 mA h/g at 2000 mA/g. The excellent lithium storage behavior can be attributed to the incorporation of $CoMoO_4$ nanoparticles into the porous *N*-doped graphitic carbon nanofibers, which efficiently buffer the volume changes of $CoMoO_4$ upon lithiation/delithiation and maintain the overall electrode conductivity/integrity.

1. Introduction

Lithium ion batteries (LIBs) have been considered as one of the most promising energy storage systems owing to their high energy density, no memory effects, long cycle life and environmental benignity, which have been extensively used in various electrical fields ranging from portable electronics such as mobile phones to large-scale devices including electric vehicles and smart-grid [1–5]. Commercial LIBs using graphite anode, which possesses a low specific theoretical capacity of only 372 mA h/g, can't satisfy the fast expanding energy-storage demand [5–8].

* Corresponding author.
E-mail address: hongkang.wang@mail.xjtu.edu.cn (H. Wang).

https://doi.org/10.1016/j.jcis.2019.06.039
0021-9797/

To fulfill the requirement on large-scale applications, development of alternative electrode materials with higher specific power and energy densities has been receiving increasing attentions [9–12].

Among various candidate anode materials, transition metal molydates have emerged as prospective materials for energy storage [13–18]. As a representative, $CoMoO_4$ has attracted great interests owing to its high theoretical capacity of 980 mA h/g [19–22]. However, the $CoMoO_4$ anode suffers from intrinsic insufficient conductivity and relatively severe volume changes upon lithiation/delithiation, which result in the poor electrochemical properties and thus hinder its practical application. To address these problems, rational structure design and efficient material synthesis have been focused in order to develop novel $CoMoO_4$ nanostructures with high energy storage capability and excellent cycling stability [23]. For example, Zhang *et al.* fabricated $CoMoO_4$ submicrometer particles with interconnected networks through thermolysis of polymer-metal precursor solution [19]. Chen *et al.* demonstrated the fabrication of hierarchical three-dimensional $CoMoO_4$/polypyrrole core-shell nanowire arrays on carbon cloth by a two-step solution based route [24]. Dong *et al.* prepared various micro/nano-structured $CoMoO_4$ via pH-dependent solvothermal approach and the as-prepared hollow hydrangea-like $CoMoO_4$ electrode displayed superior electrochemical properties [25]. All of the as-prepared $CoMoO_4$ nanostructures demonstrated great improvement on lithium storage properties, but which were all prepared *via* solution-based synthetic strategies such as hydrothermal and solvothermal methods, which showed limitations on large scale fabrication. Therefore, development of efficient synthetic route with delicate nanostructure design and easiness to scale-up is still challenging.

Electrospinning is an efficient facile technique to fabricate one-dimensional nanostructures with delicate composition control, which can be easily scaled up [26–28]. To the best of our knowledge, electrospinning has been rarely used for synthesis of $CoMoO_4$ nanostructures. Only Xu *et al.* have demonstrated the electrospinning synthesis of $CoMoO_4$(@graphene) nanofibers, but which were obtained by only annealing in air [20]. The as-obtained pure $CoMoO_4$ nanofibers can only deliver a capacity of 321 mA h/g after 85 cycles, while the $CoMoO_4$@graphene nanofibers delivered a reversible capacity of 735 mA h/g after 200 cycles at a current density of 100 mA/g. Apparently, introduction of carbon-based nanomaterials can greatly improve the lithium storage performance. It's noteworthy that the polymers used for electrospinning can be excellent carbon source, such as polyvinyl pyrrolidone (PVP) and polyacrylonitrile (PAN) with higher N content can be used for fabrication of *N*-doped carbon nanofibers with higher electric conductivity, but which can only be obtained by annealing under inert atmosphere at high temperature [29,30]. At this temperature, the as-produced carbon is reductive, which would reduce or react with the oxidized metal species and cannot be used to directly synthesis $CoMoO_4$ nanomaterials in the carbon matrices.

Herein, we successfully developed the synthesis of porous $CoMoO_4$/CNFs by electrospinning followed by a two-step annealing strategy. The first annealing under inert atmosphere allowed the carbonization of polymer forming graphitic crystalline carbon nanofibers with the *in-situ* generated transition metal nanoparticles as catalysts, while the second annealing in air allowed the oxidation of Co-Mo intermediates by consuming partial carbon matrices, which resulted in the formation of porous nanostructure. The carbon content in the $CoMoO_4$/CNFs can be tuned by the annealing temperature. When used as LIB anode, the $CoMoO_4$/CNFs demonstrated superior electrochemical behaviors due to the novel porous interconnected nanostructures.

2. Experimental section

2.1. Materials synthesis

All chemicals, including polyacrylonitrile (PAN, $(C_3H_3N)_n$, Macklin), N,N-dimethyformamide (DMF, C_3H_7NO, Macklin), cobalt(II) acetate ($C_4H_6CoO_4$, $Co(ac)_2$, Macklin) and molybdenyl acetylacetonate ($C_{10}H_{14}MoO_6$, $Mo(acac)_2$, Macklin), were used as received without any further treatment. In a typical synthesis of the $CoMoO_4$/CNFs, electrospinning and subsequent annealing were used. First, a precursor solution for electrospinning was prepared by dissolving 1.0 g PAN, 2 mmol $Co(ac)_2$ and 2 mmol $Mo(acac)_2$ in 10 mL DMF under continuous stirring, until forming a homogeneous transparent solution. Subsequently, the precursor solution was put into a plastic syringe which was equipped with a stainless steel nozzle. For electrospinning, the fiber collector (aluminum foil) was settled at about 15 cm away from the nozzle tip. A high voltage of 18 kV was applied and the flow velocity was kept at 0.5 mL/h. The as-spun precursor nanofibers was dried at 60 °C overnight and then removed from the aluminum foil, which was then transferred into a tube furnace and annealed under Ar flow at 700 °C for 2 h with a heating rate of 1 °C/min. Thus, an intermediate product of Co/MoC/CNFs were obtained, which were further transformed into $CoMoO_4$/CNFs by annealing at 400 °C for 3 h in air. Note that the carbon content can be readily tuned through controlling the annealing temperature in air. When annealing in air at 500 °C for 3 h, only nanoparticulate $CoMoO_4$ was obtained, while partially oxidized $CoMoO_x$/CNFs were obtained when annealing at 300 °C for 3 h in air.

2.2. Materials characterization

The phase structures were examined using X-ray diffraction (XRD) machine (Bruker D2 PHASER, Cu Kα radiation, λ = 1.5418 Å), operating at 30 kV and 10 mA. Scanning electron microscopy (SEM) images were obtained on a FEI Quanta 250 SEM, while transmission electron microscopy (TEM) images as well as the high-angle annular dark field (HAADF) scanning TEM (STEM) images were taken on a JEOL JEM2100 TEM equipped with energy dispersive spectrometer (EDS) at an operating voltage of 200 kV. Raman spectroscopy was performed on a Renishaw Raman RE01 spectrometer equipped with 514 nm Ar laser. X-ray photoelectron spectroscopy (XPS) was performed on a Thermo Fisher XPS instrument (ESCALAB Xi+). Thermogravimetric analysis (TGA) was conducted in air on a Mettler thermal analysis TGA/DSC system. The N_2 adsorption-desorption isotherms were obtained using an Autosorb iQ-MP surface area analyzer (Quantachrome Instruments), determined according to Brunauer-Emmett-Teller (BET) method.

2.3. Electrochemical measurements

CR2025 coin-type cells were employed to study the electrochemical properties of the products, which were assembled in an argon-filled glovebox with concentrations of both moisture and oxygen below 1.0 ppm. For fabricating the working electrodes, aqueous slurry was first prepared by mixing active materials (the mass of the active materials with average loading amount of around 1.0 mg/cm^2), acetylene black and poly acrylic acid (PAA) binder with a weight ratio of 80:10:10, which was cast on a copper foil *via* doctor-blading method, followed by drying at 120 °C overnight under vacuum. Lithium foil and microporous membrane (Celgard 2400) were used as the counter electrode and the separator, respectively. An electrolyte with 1 M $LiPF_6$ dissolved in ethylene carbonate/dimethyl carbonate (1:1 in volume) was adopted. Galvanostatic discharge–charge tests of the cells were conducted

on a NEWARE battery test system (BTS, Neware Technology Co., Ltd., China) in 0.01–3.0 V (*vs.* Li/Li^+) at 25 °C. Cyclic voltammetry (CV) was measured on an Autolab electrochemical station (PGSTAT 302 N), while electrochemical impedance spectroscopy (EIS) was measured using CHI600E electrochemical station in frequency range of 10 MHz-0.01 Hz with a voltage amplitude of 5 mV.

3. Results and discussion

Fig. 1a schematically illustrates the synthetic procedure of fibrous $CoMoO_4$/CNFs *via* electrospinning and subsequent annealing. First, precursor nanofibers of $Mo(acac)_2/Co(Ac)_2$/PAN were prepared *via* electrospinning (Fig. S1), which were subsequently annealed at 700 °C for 2 h in Ar atmosphere. During this process, PAN carbonized and then reduced or reacted with the Co/Mo sources, *in-situ* forming Co/MoC nanoparticles which were encapsulated into the carbon nanofiber matrices (denote as Co/MoC/CNFs). As shown in the XRD patterns (Fig. S2a), the diffraction peaks at 44.2°, 51.5° and 75.9° can be assigned to the metallic Co phase (JCPDS No. 15-0806), while the apparent peaks at 35.0°, 36.7°, 39.2°, 42.6°, 46.8°, 56.4°, 61.5°, and 75.3° can be related to the MoC phase (JCPDS No. 21-0384). Besides, the peak at 26.4° in the Co/MoC/CNFs may be assigned to the graphite carbon of CNFs [31]. $CoMoO_4$/CNFs were then prepared by simply annealing the Co/MoC/CNFs at 400 °C under ambient atmosphere. As revealed by the XRD pattern (Fig. S2b), all the apparent diffraction peaks well correspond to the $CoMoO_4$ phase (JCPDS No. 21-0868), indicating the reaction between Co and MoC nanoparticles in air.

The microstructures of the Co/MoC/CNFs and the $CoMoO_4$/CNFs were revealed by SEM, TEM and HRTEM analyses. As revealed by the SEM image (Fig. 1b), the Co/MoC/CNFs display well-defined one-dimensional morphology with smooth surface, and the diam-

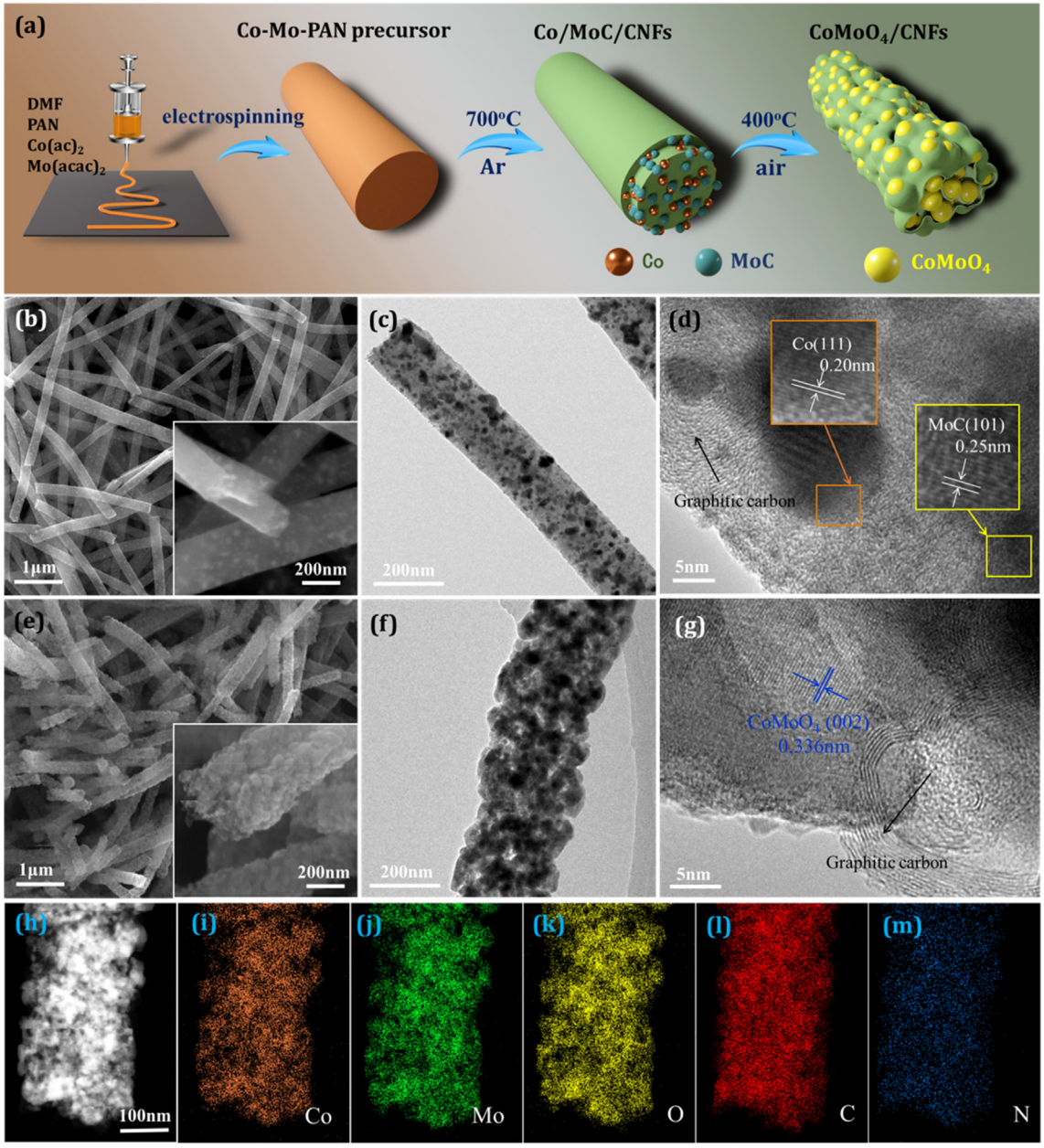

Fig. 1. (a) Schematic illustration of the synthesis of $CoMoO_4$/CNFs. (b) SEM and (c, d) TEM/HRTEM images of the intermediate Co/MoC/CNFs with inset of (d) showing the enlarged lattice fringes taken from the selected area. (e) SEM and (f, g) TEM/HRTEM images of the $CoMoO_4$/CNFs. (h) HAADF-STEM image of a single $CoMoO_4$/CNF with the corresponding elemental maps of (i) Co, (j) Mo, (k) O, (l) C and (m) N elements.

eters are in the range of 100–300 nm with lengths up to several to tens of micrometers. In the enlarged SEM image (inset of Fig. 2b), fine nanoparticles are clearly observed and fully embedded into the carbon nanofibers, which can be indexed to the Co and MoC nanoparticles, respectively. As confirmed by the TEM/HRTEM images (Fig. 1c-d), Co and MoC nanoparticles with size of several to tens of nanometers are well embedded into the solid carbon nanofiber matrices. In the HRTEM image (Fig. 2d), the interplanar spacings of 0.2 and 0.25 nm can be correspondingly assigned to the Co (1 1 1) and MoC (1 0 1) planes. In addition, the graphitic crystallization of the carbon nanofibers can also be observed.

In contrast, $CoMoO_4$/CNFs exhibit coarse surfaces after annealing Co/MoC/CNFs in air, indicating that the Co/MoC nanoparticles were oxidized and/or reacted in air, thus forming $CoMoO_4$ nanoparticles within the carbon nanofiber matrices (Fig. 1e). Moreover, the overall diameters of the $CoMoO_4$/CNFs seem to be slightly increased. Differently, the $CoMoO_4$/CNFs show distinctly porous microstructure (Fig. 1e-f), and the HRTEM image reveals the clear lattice fringes with d spacing of 0.336 nm, which corresponds to the (0 0 2) plane of $CoMoO_4$ (JCPDS No. 21-0868). Besides, the lattice fringes belonging to the graphitic carbon can also be observed in the $CoMoO_4$/CNFs. To further confirm the elemental distribution within the $CoMoO_4$/CNFs, HAADF-STEM image with corresponding EDS maps were taken, and reveal that the elemental distributions of Co, Mo and O elements are well overlapped but located within the carbon map, indicating the cross-linking and encapsulation of the $CoMoO_4$ nanoparticles by the carbon nanofibers (Fig. 1h-l). Besides, N element can also be observed, which arises from the simultaneous doping of carbon nanofibers during the carbonization of PAN, serving as a co-source of C/N.

Fig. 2a shows the phase evolution of the Co/MoC/CNFs upon annealing in air at different temperature. After annealing in air at 300 °C, the XRD pattern changes a lot but doesn't show apparent peaks, indicating the poor cystallization of the $CoMoO_x$ product. With further increasing the annealing temperature to 400 and 500 °C, the diffraction peaks emerge and become apparent with increased intensity, indicating the formation of crystalline $CoMoO_4$ product. In order to determine the carbon content in the products and the carbon evolution upon annealing in air, TAG and Raman analyses were perfomed. As shown in Fig. 2b, the Co/MoC/CNFs show an abrupt weight loss of ~44.4 wt% at ~440 °C, and the $CoMoO_x$/CNFs show similar TAG profile, indicating the material structure was slightly changed owing to the lower annealing temperature (300 °C) (Fig. S3). In the $CoMoO_4$/CNFs obtained after annealing in air at 400 °C for 3 h, the carbon content can be estimated as ~ 33.9 wt%, while the carbon was almost completely burned when annealing in air at 500 °C for 3 h. Without the presence of carbon matrices, the $CoMoO_4$ loses the fibrous morphology and exists as discrete nanoparticles (Fig. S3), indicating that the carbon nanofibers serve as a link to cross the $CoMoO_4$ nanoparticles.

Raman measurements were further conducted to reveal the existing state of carbon in the products and their evolution upon annealing in air. As shown in Raman spectra of the Co/MoC/CNFs and the counterparts obtained after annealing in air at 300 and 400 °C, two obvious peaks at around 1341 and 1589 cm^{-1} can be observed, which correspond to the disordered carbon (D) and the ordered graphitic carbon (G) [30,32], respectively. The I_D/I_G intensity ratios for Co/MoC/CNFs, $CoMoO_x$/CNFs and CoMoO4/CNFs are 1.28, 1.29 and 1.54, respectively, indicating that annealing at 400 °C in air would affect the graphitization degree owing to the

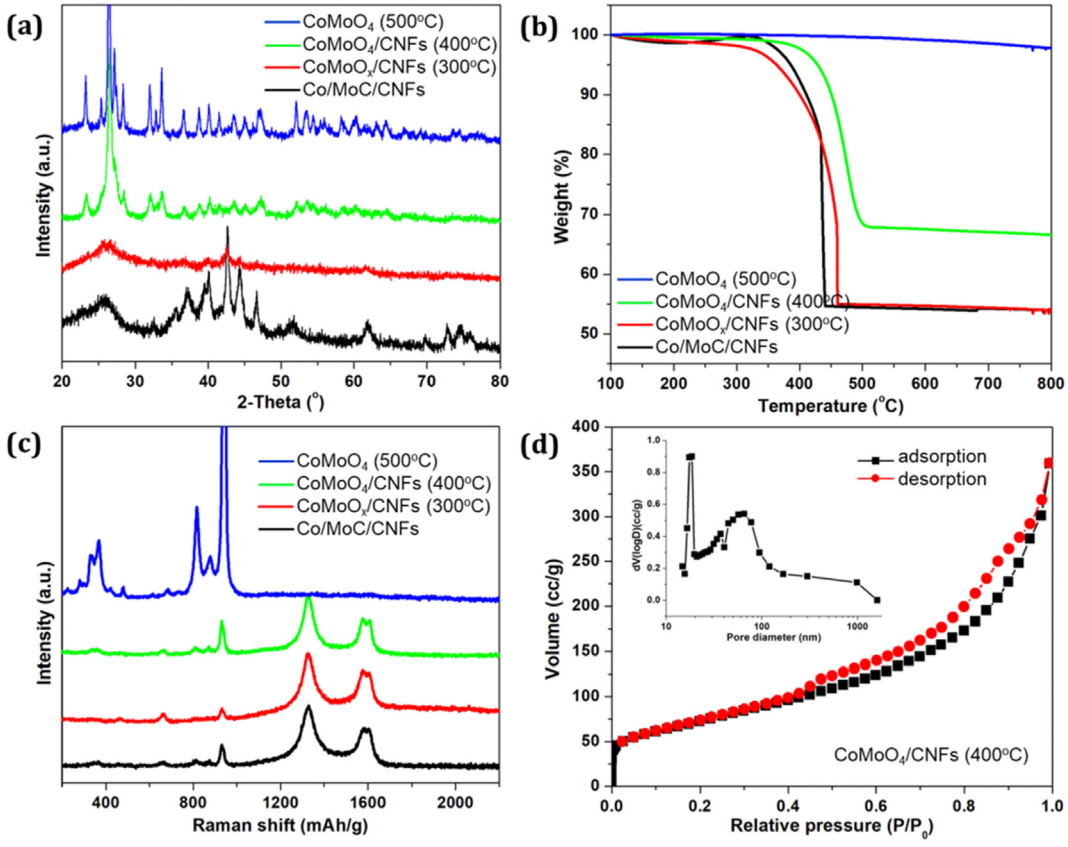

Fig. 2. (a) XRD patterns, (b) TGA curves and (c) Raman spectra of the intermediate Co/MoC/CNFs and the counterparts obtained after annealing Co/MoC/CNFs at 300, 400 and 500 °C. (d) N_2 adsorption-desorption isotherms with inset showing the pore-size distribution.

partial consumption by reacting with oxygen. In the product obtained by annealing at 500 °C in air, no peaks corresponding to carbon can be observed. Instead, the prominent peaks at 337, 367, 816, 877 and 936 cm^{-1} becomes prominent and can be indexed to the $CoMoO_4$ [6,20]. The much stronger intersnity than that in the other products indicates the higher crystallization of $CoMoO_4$ owing to the increased annealing temperature. In addtion, the porous feature of the $CoMoO_4$/CNFs was examined by N_2 adsorption-desorption isotherms, as shown in Fig. 2d. The $CoMoO_4$/CNFs exhibit a specific surface area of 255.3 m^2/g and a pore volume of 0.52 cc/g with average pore diameter of 43.5 nm, indicating the macroporous characteristics.

X-ray photoelectron spectroscopy (XPS) was used to evaluate the chemical states and the chemical compositions of the $CoMoO_4$/CNFs. Fig. 3a displays the survey XPS spectrum, revealing the presence of Co, Mo, O, N and C elements. Fig. 3b shows the Co 2p spectrum with two apparent peaks at 797.5 and 781.2 eV, which correspond to the Co $2p_{1/2}$ and Co $2p_{3/2}$, respectively. Together with the presence of the shakeup satellite peaks located at approximately 6.5 eV higher binding energy sides of the Co $2p_{1/2}$ and Co $2p_{3/2}$, it can be concluded that the Co element in the $CoMoO_4$/CNFs exists as the Co(II) oxidation state. This is consistent with the previous reports on $CoMoO_4$ [33,34]. Fig. 3c displays the core-level Mo 3d XPS spectrum with two apparent peaks at 232.7 and 235.8 eV, which can be indexed to Mo $3d_{5/2}$ and Mo $3d_{3/2}$ with the oxidation state of Mo(VI) oxidation [35–37]. The broad peak located at around 398.5 eV can be attributed to the overlapped Mo 3p3/2 and N 1s peak [26,38], indicating the *N*-doping of the carbon nanofibers, which is consistent with the EDS elemental analysis.

The electrochemical properties of $CoMoO_4$/CNFs were investigated as LIB anodes in half-cells using lithium foil as counter and reference electrode. Fig. 4a shows the CV curves of the $CoMoO_4$/CNF electrode in the first three cycles at a scan rate of 0.2 mV/s. Apparently, two reduction peaks appear in the first cathodic scan, and the distinct one at ~1.6 V can be assigned to the reduction of $CoMoO_4$ into metallic Co and Mo ($CoMoO_4 + 8Li^+ + 8e^- \rightarrow 4Li_2O + Co + Mo$) [19,20,24,39], while the sharp/broad one below 0.7 V can be attributed to the formation of solid electrolyte interphase (SEI) layer and also the lithium insertion into the carbon matrices [5]. Moreover, this broad peak below 0.7 V disappears in the follow cathodic scans, suggesting the irreversible formation of SEI film. Instead, a narrow/sharp cathodic peak near 0.01 V still presents, corresponding to the reversible lithiation of the carbon nanofibers. Since the 2nd cathodic scan onwards, the two cathodic peaks shift to 1.5 and 0.6 V, respectively, indicating the irreversible structural destruction/reorganization of the pristine $CoMoO_4$ upon initial lithiation and the reversible reduction of the oxidized Co/Mo species in the following cycles. In all the three anodic scans, two well-overlapped oxidation peaks at around 1.45 V and 1.85 V relate to the reversible oxidations of Co and Mo to CoO and MoO_3 ($Co + Li_2O \leftrightarrow CoO + 2Li^+ + 2e^-$, $Mo + 3Li_2O \leftrightarrow MoO_3 + 6Li^+ + 6e^-$) [19,20,39], respectively.

Fig. 4b shows the 1st, 2nd, 3rd and 10th discharge-charge profiles of the $CoMoO_4$/CNFs at 200 mA/g. In the first discharge profile, two plateaus at 1.6 and 0.3 V are observed, which are related to the reduction of Co^{2+}/Mo^{6+} and formation of SEI layer, and this is well consistent with the CV result. Since the second cycle onwards, only sloping plateaus can be observed in both the discharge/charge

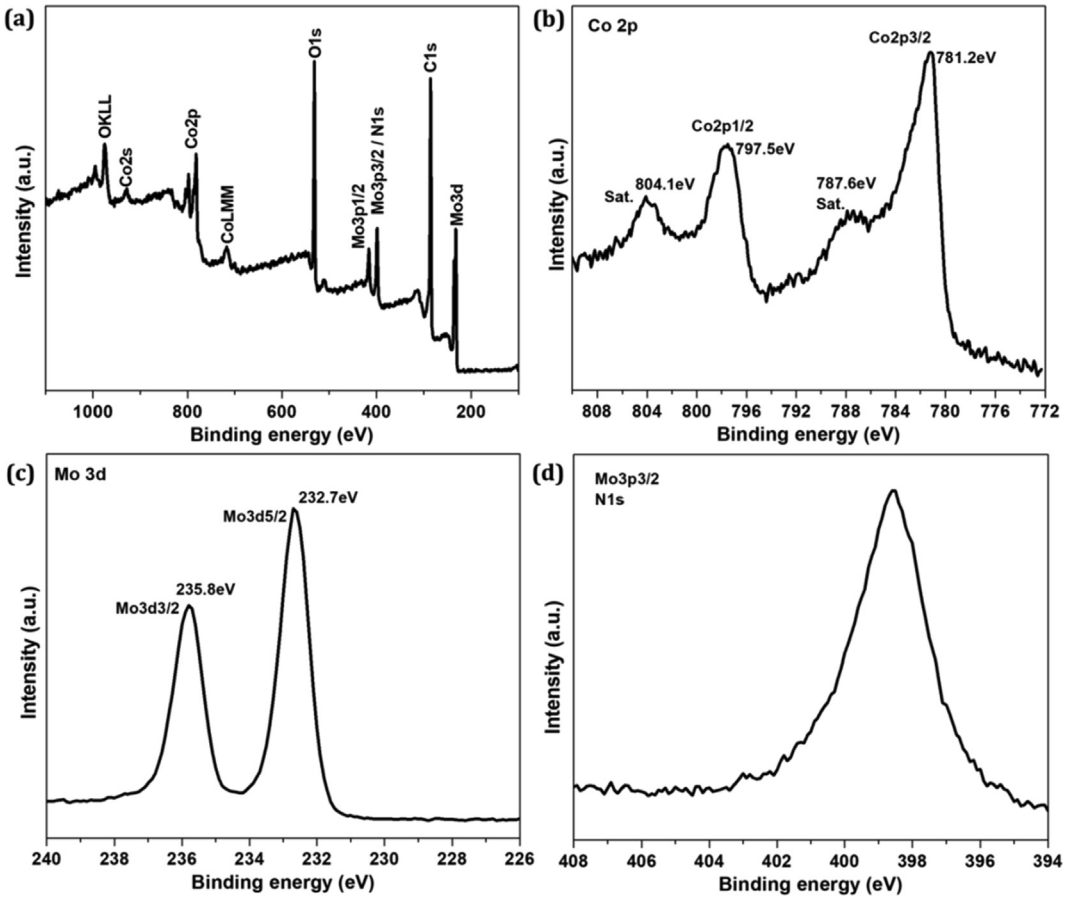

Fig. 3. (a) Survey XPS spectrum, (b) Co 2p, (c) Mo 3d and (d) Mo 3p3/2 + N 1s XPS spectra of the $CoMoO_4$/CNFs.

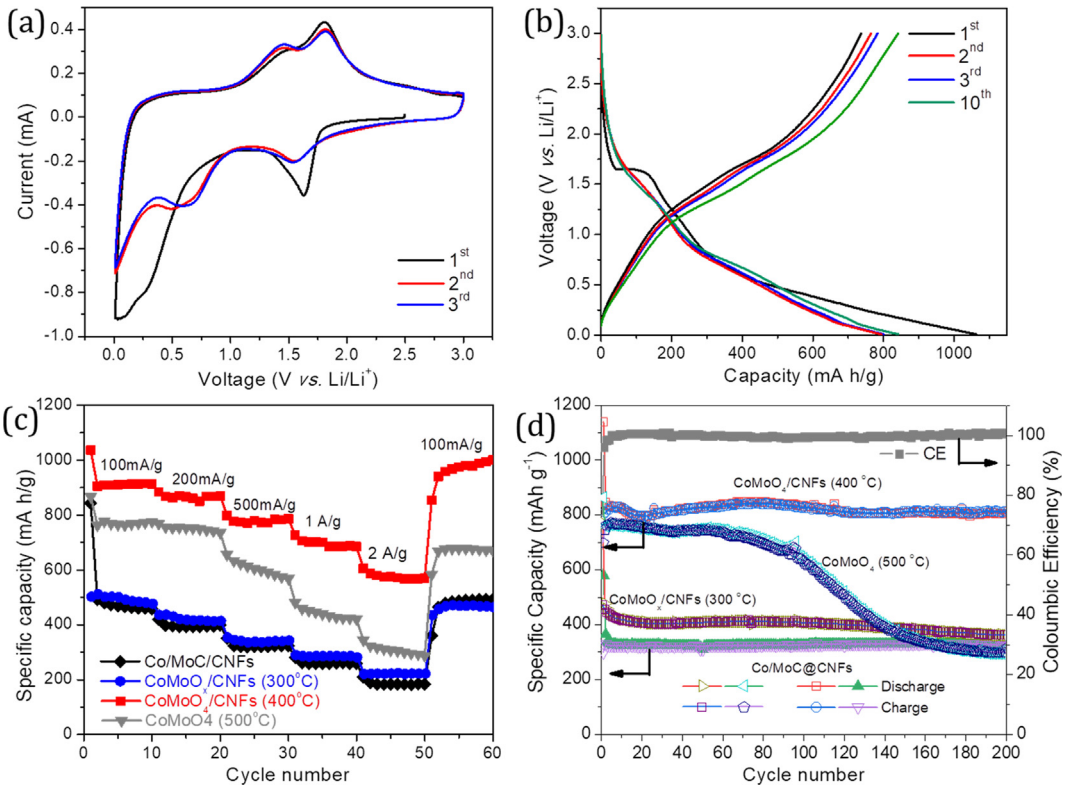

Fig. 4. (a) Cyclic voltammetry (CV) curves at 0.2 mV/s and (b) Galvanostatic discharge-charge profiles at 200 mA/g for the $CoMoO_4$/CNF electrode in 0.01–3.0 V. (c) Rate performance and (d) cycle performance of Co/MoC/CNFs and their counterpart electrodes, with (d) showing the Coulombic efficiency (CE) of the $CoMoO_4$/CNF electrode.

profiles, indicating the stepwise/multistep lithiation/delithiation reactions in the mixed Co/Mo oxides. The initial discharge and charge capacities for the $CoMoO_4$/CNF electrode are 1060 and 767 mA h/g, displaying an initial Coulombic efficiency of 72.4%. The initial capacity loss could be mainly attributed to the formation of the SEI film. Meanwhile, the discharge-charge profiles for the $CoMoO_4$/CNFs electrode at different rates are also presented in Fig. S4, in which the sloping voltage plateaus are still observed and almost maintained with increasing the current densities from 100 to 2000 mA/g, indicating the good rate capability.

Fig. 4c compares the rate performance of the Co/MoC/CNFs and their counterparts obtained after annealing in air at different temperatures. Notably, the $CoMoO_4$/CNFs obtained after annealing at 400 °C in air exhibit the best rate performance, delivering high reversible capacities of 910, 865, 780, 685 and 574 mA h/g at 100, 200, 500, 1000 and 2000 mA/g, respectively. When recovering the current density to 100 mA/g, a high capacity of 940 mA h/g can be maintained. In contrast, the Co/MoC/CNFs and the counterpart $CoMoO_x$/CNFs display similar rate performance but with much lower capacities at various current densities. Even in the pure $CoMoO_4$ nanoparticle electrode where no carbon was left, the capacities are much higher than that of the Co/MoC/CNFs and the $CoMoO_x$/CNFs, indicating the the $CoMoO_4$ mainly contributes to lithium storage capacity. However, the rate capacity of the $CoMoO_4$ nanoparticles is much worse than that of the $CoMoO_4$/CNFs, indicating that the CNFs in the $CoMoO_4$/CNFs greatly improve the electrode conductivity. Furthermore, the cycling performances of the Co/MoC/CNFs and $CoMoO_4$/CNFs are compared at 200 mA/g in 0.01–3.0 V. As shown in Fig. 4d, the $CoMoO_4$/CNF electrode delivers a reversible capacity of 802 mA h/g after 200 cycles, which is much higher than that of the Co/MoC/CNF electrode (only 319 mA h/g after 200 cycles).

Electrochemical impedance spectroscopy (EIS) was further conducted to understand the enhanced electrochemical performance of the $CoMoO_4$/CNF electrode. As shown in Fig. 5, the Nyquist plots consist of a quasi-semicircle in the high frequency region and a sloping line in the low frequency region. The semicircle in the high frequency region corresponds to the charge transfer resistance (R_{ct}) in the electrode/electrolyte interface [32,39]. The charge transfer resistances are around 180 and 200 Ω for the $CoMoO_x$/CNF and $CoMoO_4$/CNF electrodes, while the $CoMoO_4$ electrode displays a large charge transfer resistance over 1000 Ω, owing to the complete combustion of the carbon nanofiber matrices. Therefore, the presence of CNFs can greatly improve the charge transfer rate.

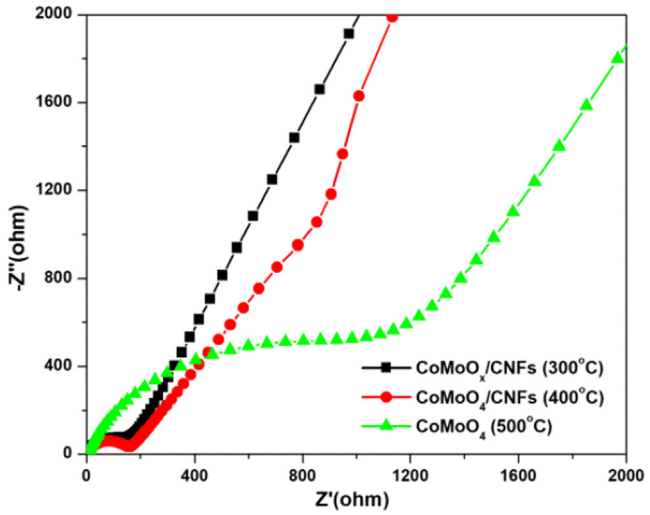

Fig. 5. Nyquist plots for the fresh $CoMoO_x$/CNF, $CoMoO_4$/CNF and $CoMoO_4$ electrodes.

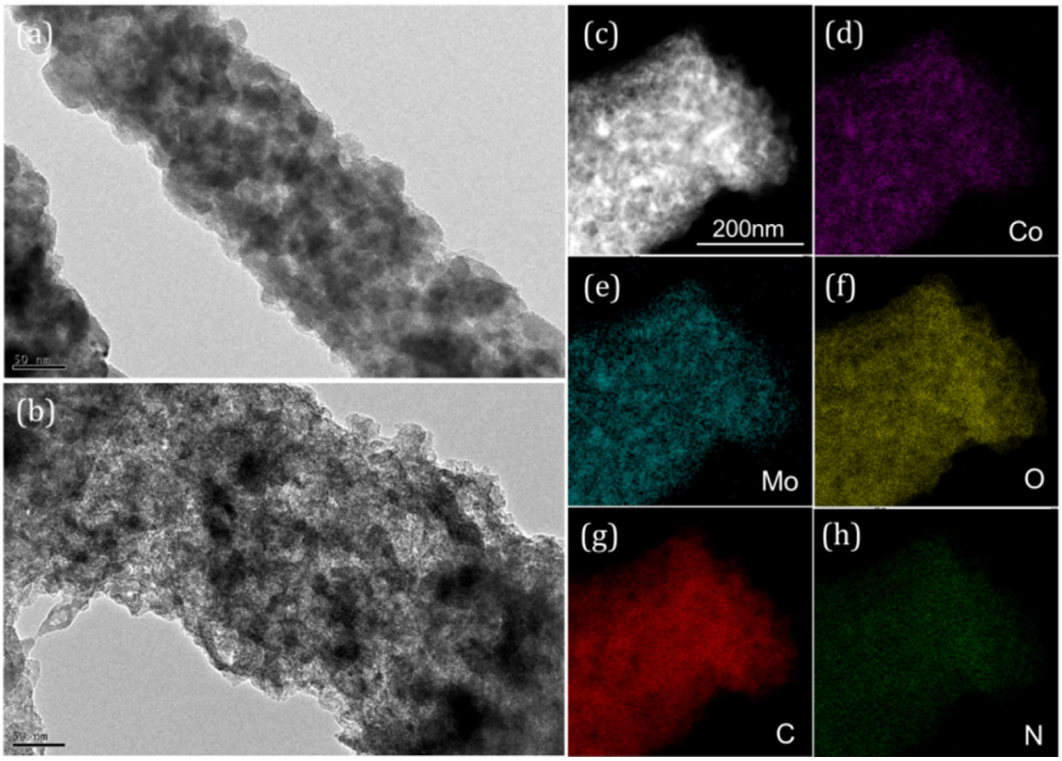

Fig. 6. (a, b) TEM images of a single $CoMoO_4$/CNF (a) and the charged counterpart (b) after 200 cycles at 200 mA/g. (c) HAADF-STEM image of a single charged $CoMoO_4$/CNF and the corresponding EDS maps of the Co (d), Mo (e), O (f), C (g) and N (h) elements.

In addition, the sharp inclined line at low frequency in the $CoMoO_4$/CNF electrode indicates the fast lithium diffusion rate in the fibrous electrodes (Fig. S5), owing to the opener frame-structures. Fig. S6 compares the Nyquist plots of $CoMoO_4$/CNF electrodes before and after cycling. Even after 200 cycles, the charge transfer resistance of the $CoMoO_4$/CNF electrode still maintained a smaller value of ~80 Ω, indicating the carbon nanofiber matrices greatly enhanced the electrode conductivity in the $CoMoO_4$/CNFs.

Ex-situ TEM analysis was also performed to investigate the structure evolution upon cycling. Fig. 6a-b compares the microstructures of a pristine $CoMoO_4$/CNF and a charged counterpart, whose fibrous morphology is well preserved. In contrast, no well-defined particle morphology within the charged fiber can be observed, indicating the amorphorization of the $CoMoO_4$ nanoparticles after lithium insertion/extraction. Fig. 6c shows the HAADF-STEM image of a single charged $CoMoO_4$/CNF, and the corresponding EDS maps were taken (Fig. 6d-h), in which Co, Mo, O, C and N elements are well distributed and overlapped within the whole fiber region, indicating the efficient buffering effect of the carbon nanofiber matrices on the lithiation-delithiation of the $CoMoO_4$ active materials.

4. Conclusions

In summary, we have demonstrated the *in-situ* formation of $CoMoO_4$ nanoparticles within porous carbon nanofibers (denote as $CoMoO_4$/CNFs), in which $CoMoO_4$ nanoparticles were cross-linked by the porous *N*-doped carbon nanofibers, *via* electrospinning and subsequent annealing under inert/air atmospheres. The annealing in inert atmosphere allowed the carbonization of the PAN with graphitic crystallization under the catalytic effect of the *in-situ* generated Co/Mo species, which were produced through carbon reduction of the Co-Mo precursors, while the further annealing in air promoted the oxidation of Co/MoC into $CoMoO_4$. The carbon content in the $CoMoO_4$/CNFs can be controlled by the annealing temperature. When applied as anode materials for lithium ion batteries, the cross-linked $CoMoO_4$/CNFs demonstrated superior lithium storage performance, delivering a high reversible capacity of 802 mA h/g after 200 cycles at 200 mA/g and a high-rate capacity of 574 mA h/g at 2000 mA/g. The enhanced electrochemical behavior of $CoMoO_4$/CNFs can be attributed to the novel structural characteristics: (i) the porous carbon nanofibers with graphitic crystallization and one-dimensional structure served as an excellent conductive matrices, which efficiently buffered the volume changes of $CoMoO_4$ upon lithium insertion/extraction, thus maintaining the overall electrode conductivity/integrity; (ii) the nanosized dimension of the embedded $CoMoO_4$ particles not only provided enlarged active sites for lithium storage but also shortened the lithium diffusion length. Besides, *ex-situ* TEM analyses clearly revealed the efficacy of such hybrid design in alleviating the volume change-induced electrode pulverization. More importantly, we presented an effective strategy to prepare mixed oxides within crystallized carbon matrices, which are promising in application as high-performance electrode materials for electrochemical energy storage.

Acknowledgments

This work was supported by the Natural Science Basis Research Plan in Shaanxi Province of China (No. 2018JM5085), State Key Laboratory for Modification of Chemical Fibers and Polymer Materials (Grant No. KF1806) of Donghua University, and the Key Laboratory Construction Program of Xi'an Municipal Bureau of Science and Technology (201805056ZD7CG40). H.W. appreciates the support of the Tang Scholar Program from the Cyrus Tang Foundation. We thank Dr. Chao Li from the Instrument Analysis Center of Xi'an Jiaotong University, and Mr Chuansheng Ma and Ms Yanzhu Dai at International Center for Dielectric Research (ICDR) of Xi'an Jiaotong University, for the help with TEM/SEM measurements.

Appendix A. Supplementary material

Supplementary data to this article can be found online at https://doi.org/10.1016/j.jcis.2019.06.039.

References

[1] D. Larcher, J.M. Tarascon, Towards greener and more sustainable batteries for electrical energy storage, Nat. Chem. 7 (2014) 19–29.
[2] N. Nitta, F. Wu, J.T. Lee, G. Yushin, Li-ion battery materials: present and future, Mater. Today 18 (5) (2015) 252–264.
[3] L. Zhao, H.-H. Wu, C. Yang, Q. Zhang, G. Zhong, Z. Zheng, H. Chen, J. Wang, K. He, B. Wang, T. Zhu, X.C. Zeng, M. Liu, M.-S. Wang, Mechanistic origin of the high performance of Yolk@Shell Bi_2S_3@N-doped carbon nanowire electrodes, ACS Nano 12 (12) (2018) 12597–12611.
[4] W. An, B. Gao, S. Mei, B. Xiang, J. Fu, L. Wang, Q. Zhang, P.K. Chu, K. Huo, Scalable synthesis of ant-nest-like bulk porous silicon for high-performance lithium-ion battery anodes, Nat. Commun. 10 (1) (2019) 1447.
[5] J. Wang, H. Wang, F. Li, S. Xie, G. Xu, Y. She, M.K.H. Leung, T. Liu, Oxidizing solid Co into hollow Co_3O_4 within electrospun (carbon) nanofibers towards enhanced lithium storage performance, J. Mater. Chem. A 7 (7) (2019) 3024–3030.
[6] T. Yang, H. Zhang, Y. Luo, L. Mei, D. Guo, Q. Li, T. Wang, Enhanced electrochemical performance of $CoMoO_4$ nanorods/reduced graphene oxide as anode material for lithium-ion batteries, Electrochim. Acta 158 (2015) 327–332.
[7] H. Wang, X. Yang, Q. Wu, Q. Zhang, H. Chen, H. Jing, J. Wang, S.-B. Mi, A.L. Rogach, C. Niu, Encapsulating silica/antimony into porous electrospun carbon nanofibers with robust structure stability for high-efficiency lithium storage, ACS Nano 12 (4) (2018) 3406–3416.
[8] H. Jiang, D.Y. Ren, H.F. Wang, Y.J. Hu, S.J. Guo, H.Y. Yuan, P.J. Hu, L. Zhang, C.Z. Li, 2D monolayer MoS_2-carbon interoverlapped superstructure: engineering ideal atomic interface for lithium ion storage, Adv. Mater. 27 (24) (2015) 3687–3695.
[9] J.B. Goodenough, K.-S. Park, The Li-Ion rechargeable battery: a perspective, J. Am. Chem. Soc. 135 (4) (2013) 1167–1176.
[10] Z. Deng, H. Jiang, Y. Hu, Y. Liu, L. Zhang, H. Liu, C. Li, 3D ordered macroporous MoS_2@C nanostructure for flexible Li-Ion batteries, Adv. Mater. (2017). 1603020-n/a.
[11] Q. Zhang, H. Chen, L. Luo, B. Zhao, H. Luo, X. Han, J. Wang, C. Wang, Y. Yang, T. Zhu, M. Liu, Harnessing the concurrent reaction dynamics in active Si and Ge to achieve high performance lithium-ion batteries, Energy Environ. Sci. 11 (3) (2018) 669–681.
[12] Z. Zheng, H.-H. Wu, H. Chen, Y. Cheng, Q. Zhang, Q. Xie, L. Wang, K. Zhang, M.-S. Wang, D.-L. Peng, X.C. Zeng, Fabrication and understanding of Cu_3Si-Si@carbon@graphene nanocomposites as high-performance anodes for lithium-ion batteries, Nanoscale 10 (47) (2018) 22203–22214.
[13] L.-Q. Mai, F. Yang, Y.-L. Zhao, X. Xu, L. Xu, Y.-Z. Luo, Hierarchical $MnMoO_4$/$CoMoO_4$ heterostructured nanowires with enhanced supercapacitor performance, Nat. Commun. 2 (2011) 381.
[14] Y. Zhao, X.F. Li, B. Yan, D.B. Xiong, D.J. Li, S. Lawes, X.L. Sun, Recent developments and understanding of novel mixed transition-metal oxides as anodes in lithium ion batteries, Adv. Energy Mater. 6 (8) (2016) 1502175.
[15] Y. Yang, S.T. Wang, C.H. Jiang, Q.C. Lu, Z.L. Tang, X. Wang, Controlled synthesis of hollow co-mo mixed oxide nanostructures and their electrocatalytic and lithium storage properties, Chem. Mater. 28 (7) (2016) 2417–2423.
[16] H. Yu, C. Guan, X.H. Rui, B. Ouyang, B. Yadian, Y.Z. Huang, H. Zhang, H.E. Hoster, H.J. Fan, Q.Y. Yan, Hierarchically porous three-dimensional electrodes of $CoMoO_4$ and $ZnCo_2O_4$ and their high anode performance for lithium ion batteries, Nanoscale 6 (18) (2014) 10556–10561.
[17] X.Z. Yu, B.G. Lu, Z. Xu, Super long-life supercapacitors based on the construction of nanohoneycomb- like strongly coupled $CoMoO_4$-3D graphene hybrid electrodes, Adv. Mater. 26 (7) (2014). 990–990.
[18] J.H. Ahn, G.D. Park, Y.C. Kang, J.H. Lee, Phase-pure beta-$NiMoO_4$ yolk-shell spheres for high-performance anode materials in lithium-ion batteries, Electrochim. Acta 174 (2015) 102–110.
[19] C.T. Cherian, M.V. Reddy, S.C. Haur, B.V.R. Chowdari, Interconnected network of $CoMoO_4$ submicrometer particles as high capacity anode material for lithium ion batteries, ACS Appl. Mat. Interfaces 5 (3) (2013) 918–923.
[20] J. Xu, S.Z. Gu, L. Fan, P. Xu, B.G. Lu, Electrospun lotus root-like $CoMoO_4$@graphene nanofibers as high-performance anode for lithium ion batteries, Electrochim. Acta 196 (2016) 125–130.
[21] Y.Y. Chen, Y. Wang, X.P. Shen, R. Cai, H.X. Yang, K.Q. Xu, A.H. Yuan, Z.Y. Ji, Cyanide-metal framework derived $CoMoO_4$/Co_3O_4 hollow porous octahedrons as advanced anodes for high performance lithium ion batteries, J. Mater. Chem. A 6 (3) (2018) 1048–1056.
[22] D.H. Lyu, L.L. Zhang, H.X. Wei, H.B. Geng, H.W. Gu, Synthesis of graphene wrapped porous $CoMoO_4$ nanospheres as high-performance anodes for rechargeable lithium-ion batteries, RSC Adv. 7 (81) (2017) 51506–51511.
[23] L. Wang, X. Cui, L. Gong, Z. Lyu, Y. Zhou, W. Dong, J. Liu, M. Lai, F. Huo, W. Huang, M. Lin, W. Chen, Synthesis of porous $CoMoO_4$ nanorods as a bifunctional cathode catalyst for a Li–O2 battery and superior anode for a Li-ion battery, Nanoscale 9 (11) (2017) 3898–3904.
[24] Y.P. Chen, B.R. Liu, W. Jiang, Q. Liu, J.Y. Liu, J. Wang, H.S. Zhang, X.Y. Jing, Coaxial three-dimensional $CoMoO_4$ nanowire arrays with conductive coating on carbon cloth for high-performance lithium ion battery anode, J. Power Sources 300 (2015) 132–138.
[25] G. Dong, H. Zhao, Y. Xu, X. Zhang, X. Cheng, S. Gao, L. Huo, Hollow hydrangea-like and hollow spherical $CoMoO_4$ micro/nano-structures: pH-dependent synthesis, formation mechanism, and enhanced lithium storage performance, J. Alloys Compd. 785 (2019) 563–572.
[26] X. Lu, P. Wang, K. Liu, C. Niu, H. Wang, Encapsulating nanoparticulate Sb/MoO_x into porous carbon nanofibers via electrospinning for efficient lithium storage, Chem. Eng. J. 336 (2018) 701–709.
[27] X. Li, J.T. Xu, L. Mei, Z.J. Zhang, C.Y. Cui, H.K. Liu, J.M. Ma, S.X. Dou, Electrospinning of crystalline MoO_3@C nanofibers for high-rate lithium storage, J. Mater. Chem. A 3 (7) (2015) 3257–3260.
[28] Y. Yu, L. Gu, C.L. Wang, A. Dhanabalan, P.A. van Aken, J. Maier, Encapsulation of Sn@carbon nanoparticles in bamboo-like hollow carbon nanofibers as an anode material in lithium-based batteries, Angew. Chem. Int. Ed. 48 (35) (2009) 6485–6489.
[29] Y.M. Sun, R.B. Sills, X.L. Hu, Z.W. Seh, X. Xiao, H.H. Xui, W. Luo, H.Y. Jin, Y. Xin, T. Q. Li, Z.L. Zhang, J. Zhou, W. Cai, Y.H. Huang, Y. Cui, A Bamboo-inspired nanostructure design for flexible, foldable, and twistable energy storage devices, Nano Letters 15 (6) (2015) 3899–3906.
[30] H. Wang, X. Lu, L. Li, B. Li, D. Cao, Q. Wu, Z. Li, G. Yang, B. Guo, C. Niu, Synthesis of SnO_2 versus Sn crystals within N-doped porous carbon nanofibers via electrospinning towards high-performance lithium ion batteries, Nanoscale 8 (14) (2016) 7595–7603.
[31] H. Wang, J. Wang, D. Cao, H. Gu, B. Li, X. Lu, X. Han, A.L. Rogach, C. Niu, Honeycomb-like carbon nanoflakes as a host for SnO_2 nanoparticles allowing enhanced lithium storage performance, J. Mater. Chem. A 5 (15) (2017) 6817–6824.
[32] Y. Li, X. Lu, H. Wang, C. Xie, G. Yang, C. Niu, Growth of ultrafine sno_2 nanoparticles within multiwall carbon nanotube networks: non-solution synthesis and excellent electrochemical properties as anodes for lithium ion batteries, Electrochim. Acta 178 (2015) 778–785.
[33] B. Wang, S. Li, X. Wu, J. Liu, W. Tian, J. Chen, Self-assembly of ultrathin mesoporous $CoMoO_4$ nanosheet networks on flexible carbon fabric as a binder-free anode for lithium-ion batteries, New J. Chem. 40 (3) (2016) 2259–2267.
[34] J. Liang, Z. Fan, S. Chen, S. Ding, G. Yang, Hierarchical $NiCo_2O_4$ nanosheets@halloysite nanotubes with ultrahigh capacitance and long cycle stability as electrochemical pseudocapacitor materials, Chem. Mater. 26 (15) (2014) 4354–4360.
[35] W. Wang, J. Qin, Z. Yin, M. Cao, Achieving fully reversible conversion in MoO_3 for lithium ion batteries by rational introduction of $CoMoO_4$, ACS Nano 10 (11) (2016) 10106–10116.
[36] S. Xie, D. Cao, Y. She, H. Wang, J.W. Shi, M.K.H. Leung, C. Niu, Atomic layer deposition of TiO_2 shells on MoO_3 nanobelts allowing enhanced lithium storage performance, Chem. Commun. 54 (56) (2018) 7782–7785.
[37] D. Cao, H. Wang, B. Li, C. Li, S. Xie, A.L. Rogach, C. Niu, Hydrothermal synthesis of SnO_2 embedded MoO_{3-x} nanocomposites and their synergistic effects on lithium storage, Electrochim. Acta 216 (2016) 79–87.
[38] J. Hou, C. Cao, F. Idrees, X. Ma, Hierarchical porous nitrogen-doped carbon nanosheets derived from silk for ultrahigh-capacity battery anodes and supercapacitors, ACS Nano 9 (3) (2015) 2556–2564.
[39] J.Y. Yao, Y.J. Gong, S.B. Yang, P. Xiao, Y.H. Zhang, K. Keyshar, G.L. Ye, S. Ozden, R. Vajtai, P.M. Ajayan, $CoMoO_4$ nanoparticles anchored on reduced graphene oxide nanocomposites as anodes for long-life lithium-ion batteries, ACS Appl. Mat. Interfaces 6 (22) (2014) 20414–20422.